Engineering 3 (2017) 701–707

Contents lists available at ScienceDirect

Engineering

journal homepage: www.elsevier.com/locate/eng

Research
Additive Manufacturing—Article

Modeling and Experimental Validation of the Electron Beam Selective Melting Process

Wentao Yan [a,b], Ya Qian [a], Weixin Ma [c], Bin Zhou [a], Yongxing Shen [c], Feng Lin [a,*]

[a] Department of Mechanical Engineering, Tsinghua University, Beijing 100084, China
[b] Department of Mechanical Engineering, Northwestern University, Evanston, IL 60201, USA
[c] State Key Lab of Metal Matrix Composites, Shanghai Jiao Tong University, Shanghai 200240, China

ARTICLE INFO

Article history:
Received 15 May 2017
Revised 25 September 2017
Accepted 27 September 2017
Available online 25 October 2017

Keywords:
Modeling
Electron beam
Additive manufacturing
Powder scale

ABSTRACT

Electron beam selective melting (EBSM) is a promising additive manufacturing (AM) technology. The EBSM process consists of three major procedures: ① spreading a powder layer, ② preheating to slightly sinter the powder, and ③ selectively melting the powder bed. The highly transient multi-physics phenomena involved in these procedures pose a significant challenge for *in situ* experimental observation and measurement. To advance the understanding of the physical mechanisms in each procedure, we leverage high-fidelity modeling and post-process experiments. The models resemble the actual fabrication procedures, including ① a powder-spreading model using the discrete element method (DEM), ② a phase field (PF) model of powder sintering (solid-state sintering), and ③ a powder-melting (liquid-state sintering) model using the finite volume method (FVM). Comprehensive insights into all the major procedures are provided, which have rarely been reported. Preliminary simulation results (including powder particle packing within the powder bed, sintering neck formation between particles, and single-track defects) agree qualitatively with experiments, demonstrating the ability to understand the mechanisms and to guide the design and optimization of the experimental setup and manufacturing process.

1. Introduction

Electron beam selective melting (EBSM) is a promising additive manufacturing (AM) technology for metallic components. It is capable of manufacturing components with complex geometry, and opens up new avenues for locally manipulating chemical compositions and mechanical properties as well. For example, Yang et al. [1] manufactured auxetic lattice structures with negative Poisson's ratios, and Ge et al. [2–4] manufactured functionally graded Ti-TiAl materials.

There are three main fabrication procedures in EBSM [2], as shown in Fig. 1.

(1) Spread one layer of powder on a preheated platform or previous layer. The layer thickness can vary for different layers. For each layer, the mixture ratio of the several different types of powder can be designed and tailored in order to allow the chemical compositions to be manipulated.

(2) Preheat the powder bed to make the powder slightly sintered. This helps prevent powder scattering, which may even lead to build failure.

(3) Selectively melt the powder bed. The beam power and scan speed are key factors that greatly influence the final part quality.

Although the basic principle of EBSM is rather straightforward, the actual processes consist of multiple physical phenomena such as powder particle packing, heat transfer, phase transformation, and fluid flow, and a number of factors influence the process and fabrication quality. There are a considerable number of fundamental physical mechanisms in each fabrication procedure to be understood

* Corresponding author.
E-mail address: linfeng@tsinghua.edu.cn

http://dx.doi.org/10.1016/J.ENG.2017.05.021

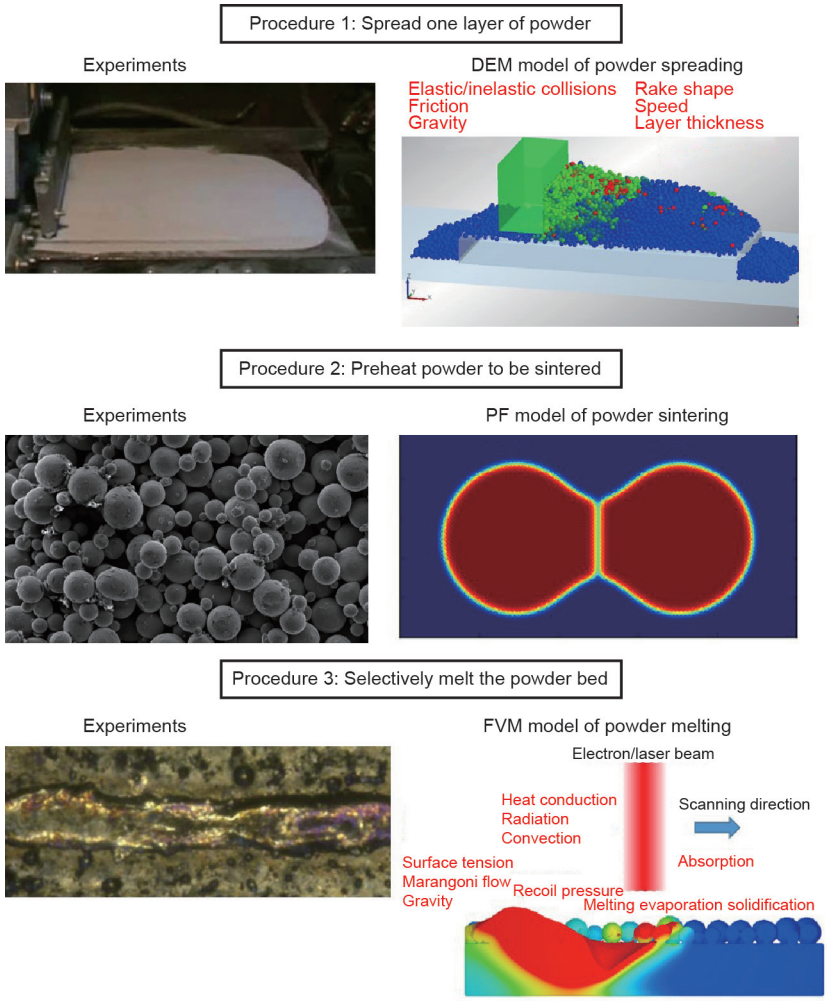

Fig. 1. Experiments and models of all procedures in the EBSM process. DEM: discrete element method; PF: phase field; FVM: finite volume method.

in order for optimal process parameters to be selected to ensure the fabrication quality. For example, the questions of how to improve the packing density of the powder bed in the powder-spreading procedure, how to achieve the optimal coalescence state of the powder bed in the preheating procedure, and how to avoid the balling effect and reduce single-track non-uniformity are all meaningful research topics.

Most previous studies focused on the melting procedure rather than on the other two procedures. Few studies have been done to comprehensively model all the manufacturing procedures. A few powder-scale models resolving the randomly distributed particles in the powder bed have been developed to investigate the melting process of individual powder particles [5–7]. Körner et al. [5] employed the rain model to generate the powder layer and the two-dimensional (2D) lattice Boltzmann method (LBM) to model the powder-melting process. They studied the influence of the powder layer thickness and input energy on the successive consolidation process of multiple powder layers. Khairallah et al. [6] built a meso-scopic model for selective laser melting (SLM) in order to investigate the formation mechanism of pores, spatter, and denudation in the single-track formation process using the ALE3D multi-physics code. Qiu et al. [8] used the open-source code OpenFOAM to simulate the powder-scale melt flow in the SLM process in order to study the surface structure and porosity development. These models incorporated most of the driving forces of the molten pool flow, including surface tension, the Marangoni effect, and recoil pressure. In this work, we leverage modeling and experiments to advance the understanding of physical mechanisms in each of the three procedures (Fig. 1). The models are introduced in Section 2, and include a powder-spreading model using the discrete element method (DEM), a phase field (PF) model of powder sintering, and a powder-melting model using the finite volume method (FVM). Section 3 presents the experimental methods. In Section 4, experimental and simulation results for each procedure are presented and discussed. Finally, a brief summary is given in Section 5.

2. Models

Note that the notations in the three subsections apply only in the respective subsections.

2.1. Powder-spreading model

Spherical powder particles with diameters that follow a Gaussian distribution in the range of 30–50 μm firstly fall to the bottom under gravity to form a powder bed, covering the substrate with various thicknesses. The rake then moves from left to right to spread the powder (Fig. 1). The movement of powder particles is governed by the contact interaction and body forces.

The Hertz-Mindlin contact model is used. In a simple case where there are only two contact particles with radii R_1 and R_2, the contact forces in the normal and tangential directions consist of nonlinear deformation and damping, as given in Eq. (1) and Eq. (2).

$$\boldsymbol{F}_{\mathrm{n}} = \left(-K_{\mathrm{n}}\delta_{\mathrm{n}}^{3/2} - \gamma_{\mathrm{n}}\left|\dot{\delta}_{\mathrm{n}}\right|\right)\boldsymbol{e}_{\mathrm{n}} \tag{1}$$

$$\boldsymbol{F}_{\mathrm{t}} = -\left(K_{\mathrm{t}}\left|\xi_{\mathrm{t}}\right| + \gamma_{\mathrm{t}}\left|\dot{\xi}_{\mathrm{t}}\right|\right)\boldsymbol{e}_{\mathrm{t}} \tag{2}$$

where δ_{n} and $|\xi_{\mathrm{t}}|$, and $|\dot{\delta}_{\mathrm{n}}|$ and $|\dot{\xi}_{\mathrm{t}}|$ are the relative displacements and velocities in the normal ($\boldsymbol{e}_{\mathrm{n}}$) and tangential ($\boldsymbol{e}_{\mathrm{t}}$) directions, respectively; while K_{n} and K_{t}, and γ_{n} and γ_{t} are the effective stiffnesses and damping coefficients in the normal and tangential directions, respectively, given in Eq. (3).

$$\begin{cases} K_{\mathrm{n}} = \dfrac{2E}{3\left(1-\upsilon^2\right)}\sqrt{\dfrac{R_1R_2}{R_1+R_2}} \\ K_{\mathrm{t}} = \dfrac{2E}{(2+\upsilon)(1-\upsilon)}\sqrt{\dfrac{R_1R_2}{R_1+R_2}\delta_{\mathrm{n}}} \\ \gamma_{\mathrm{n}} = -\sqrt{\dfrac{5}{6}}\cdot\dfrac{\ln(\theta)}{\sqrt{\ln^2(\theta)+\pi^2}}\cdot\sqrt{3K_{\mathrm{n}}\dfrac{m_1m_2}{m_1+m_2}} \\ \gamma_{\mathrm{t}} = -\sqrt{\dfrac{5}{6}}\cdot\dfrac{\ln(\theta)}{\sqrt{\ln^2(\theta)+\pi^2}}\cdot\sqrt{2K_{\mathrm{t}}\dfrac{m_1m_2}{m_1+m_2}} \end{cases} \tag{3}$$

where E, υ, and θ are the Young's modulus, Poisson's ratio, and restitution coefficient, respectively.

If $\left|E_{\mathrm{t}}|\xi_{\mathrm{t}}| + \gamma_{\mathrm{t}}|\dot{\xi}_{\mathrm{t}}|\right| > \mu|F_{\mathrm{n}}|$, tangential slide will happen, and then the tangential force is the maximum friction as given in Eq. (4).

$$\boldsymbol{F}_{\mathrm{t}} = -\mu\left|\boldsymbol{F}_{\mathrm{n}}\right|\boldsymbol{e}_{\mathrm{t}} \tag{4}$$

where μ is the fraction coefficient.

In addition to the contact repulsive force, the cohesive nature of fine particles exhibits an attractive force. Here we use the Johnson-Kendall-Roberts (JKR) cohesion model originally implemented to incorporate the Van der Waals forces between fine and dry particles, as given in Eq. (5). The cohesion force is mainly determined by the surface energy density, Ψ, of the material.

$$\boldsymbol{F}_{\mathrm{JKR}} = 4\sqrt{\frac{\pi a^3\Psi E}{2\left(1-\upsilon^2\right)}}\boldsymbol{e}_{\mathrm{t}} \tag{5}$$

where a is the radius of the contact area.

2.2. Phase field model of powder sintering

It should be emphasized that the powder-sintering mechanism during the preheating procedure is solid-state sintering driven mainly by grain boundary diffusion, rather than liquid-state sintering driven by melting and solidification. This solid-state sintering during the preheating procedure in EBSM has rarely been studied or modeled. Thus, we propose to use the PF to model the powder sintering. For brevity, we explain the method in the case of two particles, in which case two kinds of fields are used: the volume of solid, c, and the order parameter fields, η_1 and η_2. The value of all these fields falls between 0 and 1, as illustrated in Fig. 2. Note that on the grain boundary, c = 1.

The evolution of the sintering process is driven by minimizing the total free energy, F [9]:

$$F = \int_v\left[f\left(c;\eta_1,\eta_2\right) + \frac{1}{2}\kappa_c\left|\nabla c\right|^2 + \frac{1}{2}\kappa_\eta\left|\nabla\eta_1\right|^2 + \frac{1}{2}\kappa_\eta\left|\nabla\eta_2\right|^2\right]\mathrm{d}v \tag{6}$$

where v is the volume; f is the bulk free energy; and κ_c and κ_η are gradient energy parameters. Thus, we have the Cahn-Hilliard equation for the conserved field, c:

$$\frac{\partial c}{\partial t} = \nabla\cdot\left[\boldsymbol{M}\cdot\nabla\frac{\delta F}{\delta c(\boldsymbol{x},t)}\right] = \nabla\cdot\left[\boldsymbol{M}\cdot\nabla\left(\frac{\partial f}{\partial c} - \kappa_c\nabla^2 c\right)\right] \tag{7}$$

and the Allen-Cahn equation for the non-conservative order parameter field:

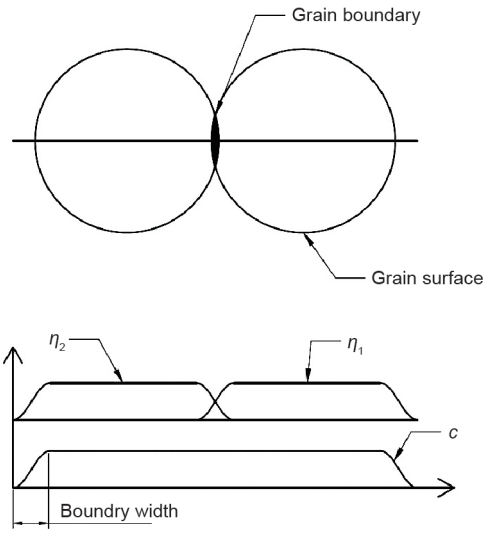

Fig. 2. Schematic of the fields in the PF model.

$$\frac{\partial\eta_\alpha}{\partial t} = -L\frac{\delta F}{\delta\eta_\alpha(\boldsymbol{x},t)} = -L\left(\frac{\partial f}{\partial\eta_\alpha} - \kappa_\eta\nabla^2\eta_\alpha\right),\ \alpha = 1,2 \tag{8}$$

where $\boldsymbol{M}$ is the concentration mobility tensor; L is the order parameter scalar mobility; $\boldsymbol{x}$ is the spatial position vector; and t represents time.

The package FEniCS [10] is adopted to solve this nonlinear problem. The Newton solver and the monolithic method are applied. Since the preheating procedure for each powder layer usually takes about 20 s, a constant time-step dt = 2 × 10^{-4} s is adopted, which should be sufficient to resolve this solid-state sintering process. Periodic boundary conditions are applied and an implicit solver is employed.

2.3. Hydrodynamic model of powder melting

The powder-melting process is governed by continuity (Eq. (9)), energy conservation (Eq. (10)), and momentum conservation (Eq. (11)), which are described in detail as follows:

$$\nabla\cdot\left(\rho\boldsymbol{v}\right) = 0 \tag{9}$$

where ρ and $\boldsymbol{v}$ denote the mass density and velocity vector of melt flow, respectively. In this study, the melted material flow is assumed to be Newtonian incompressible flow, and the mass density is set to be constant.

$$\frac{\partial(\rho I)}{\partial t} + \nabla\cdot\left(\rho\boldsymbol{v}I\right) = q + \nabla\cdot\left(k\nabla T\right) \tag{10}$$

where k is the thermal conductivity; T is the temperature; and $I = cT + (1-f_s)L$ is the specific internal energy, in which c and L are the specific heat and latent heat of melting, respectively, and f_s is the fraction of the solid. Most importantly, q is the input heat source model, which is established based on the Monte Carlo simulations of electron-atom interactions [11]. The heat source model is material dependent and experimental setup specific. Detailed descriptions are provided in our previous papers [11–13]. The initial condition is a uniform temperature distribution of 873 K, in order to incorporate the preheating procedure. The thermal boundary conditions are surface radiation and heat loss due to surface evaporation.

$$\frac{\partial(\rho\boldsymbol{v})}{\partial t} + \nabla\cdot\left(\rho\boldsymbol{v}\otimes\boldsymbol{v}\right) = \nabla\cdot\left(\mu\nabla\boldsymbol{v}\right) - \nabla p + \rho\boldsymbol{g} + \boldsymbol{f}_{\mathrm{B}} \tag{11}$$

where $\boldsymbol{g}$ denotes the gravitational acceleration vector; μ is the viscosity;

and p is the pressure. The buoyancy $\boldsymbol{f}_B$ is accounted for using the Boussinesq approximation (Eq. (12)).

$$\boldsymbol{f}_B = \rho \boldsymbol{g} \beta (T - T_0) \tag{12}$$

where β is the thermal expansion coefficient; and T_0 is the reference temperature.

The free surface is tracked using the volume-of-fluid (VOF) method. As given in Eq. (13), the phase fraction (F) in each cell is calculated, while the velocity ($\boldsymbol{v}$) is obtained from the solution of the momentum equation given by Eq. (11). Based on the phase fraction, the free surfaces can be reconstructed in each time-step.

$$\frac{\partial F}{\partial t} + \nabla \cdot (F\boldsymbol{v}) = 0 \tag{13}$$

The recoil pressure, surface tension, and Marangoni effect are treated as the boundary conditions on the free surface, while the surface tension coefficient is set to be temperature dependent.

3. Experimental methods

The EBSM system used in the study (Fig. 3) is open-architecture, which allows users to customize a wide variety of fabrication parameters. A detailed description can be found in a previous paper [4]. Since there are two powder tanks, the equipment is capable of manufacturing functionally graded materials by tailoring the mixture ratio of the two types of powder in each layer.

For the powder-spreading experiments, both the translational speed and the slope angle of the powder rake can be customized. The powder size distribution is measured using the laser particle size analyzer.

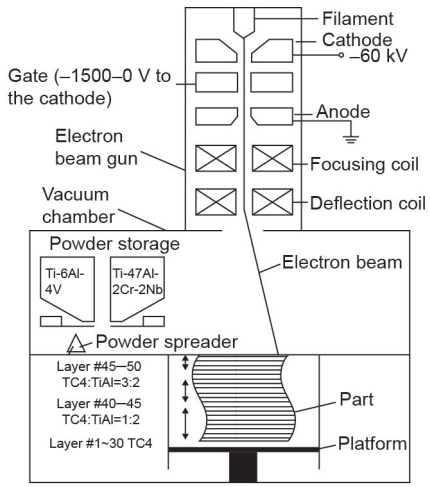

(a)

(b)

Fig. 3. The in-house EBSM system. (a) Schematic; (b) photograph.

After the powder bed is applied and before the selective melting procedure, the powder layer is usually preheated using a de-focused electron beam. The purpose is to slightly sinter powder particles together in order to avoid powder "smoke." In the post-process experimental characterization, in order to investigate the mechanism of sintering, we attached the sintered powder particles to some embedding resins at 100 °C, and then employed a focused ion beam (FIB) instrument to do the polishing. Finally, we used a scanning electron microscope (SEM) to observe the microstructures at the sintering neck at the contact point of the powder particles. Mechanical polishing is not feasible, since it may break the neck and change the microstructure.

In the powder-melting procedure, a focused electron beam is used. The morphology of single tracks is observed under an optical microscope (OM).

4. Results and discussion

4.1. Powder spreading

A good index to evaluate the performance of powder-spreading machinery is the relative packing density of the powder bed. A more compacted powder bed is usually beneficial to the fabrication quality, which can be demonstrated by the powder-melting model, as introduced in Section 2.3.

The simulations (Fig. 4(a)) can guide the design and optimization of the powder rake (Fig. 4(b)), including the rake shape and its translational speed. The relative packing density over either a flat substrate or the fluctuating surface of previous layers can be predicted (Fig. 4(c)) and then compared with experiments (Fig. 4(d)).

Some preliminary simulation results reveal the following phenomena:

- If the translational speed is relatively low, the rake shape does not affect the packing density, and the resultant packing density is high.
- The packing density decreases with the increase of the rake speed, as illustrated in Fig. 5. It should be noted that the effect of rake vibration is not incorporated into the current model; however, in experiments, the vibration is influenced by the rake speed, and then in turn influences the powder spreading [4]. It should also be mentioned that the first powder layer has a lower packing density than that of the whole powder bed, since the layer thickness is only around two times the mean powder particle diameter.

4.2. Powder sintering

The PF modeling of sintering is primarily in 2D. Two simulation cases are presented: ① two powder particles with different sizes, and ② two powder particles with similar sizes (Fig. 6). In Fig. 6(a) and Fig. 6(c), the red portion denotes the domain full of material, the blue portion denotes the domain without material, and transitional colors represent the material interfaces. Table 1 [14–16] lists some material parameters applied.

Although there are still quite a few improvements to be made to this model, the experimental observation (Fig. 6(b) and Fig. 6(d)) has been qualitatively reproduced, which demonstrates the modeling ability of the proposed method for the sintering process. It should be noted that the scales are different between the modeling and the experiment. To reach the same sintering stage, a larger scale will result in a much longer time, due to the size effect.

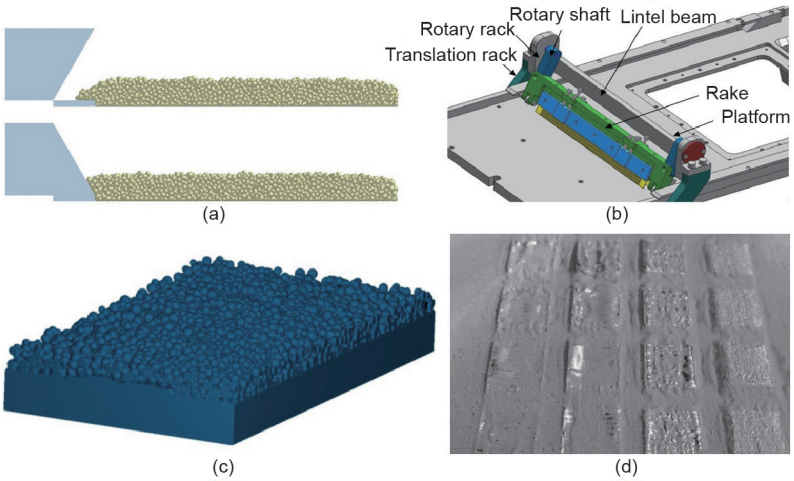

Fig. 4. Experimental and simulation results of powder spreading. (a) Simulations can guide the design and optimization of the (b) powder rake; (c) simulation and (d) experimental results of spreading a powder layer over previous layers.

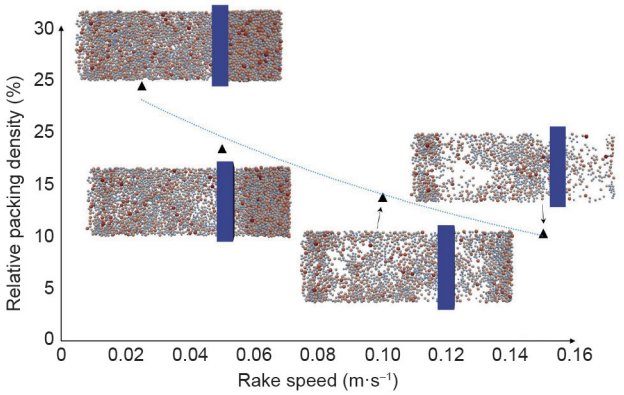

Fig. 5. Powder-spreading simulation results at various rake speeds.

Table 1
Material parameters applied in the powder-sintering simulation.

Property	Value	Unit
Grain boundary mobility, ϑ_{gb}	10^{-11}	$m^4 \cdot (J \cdot s)^{-1}$
Grain boundary energy, γ_{gb} [14]	0.81	$J \cdot m^{-2}$
Surface energy, γ_{sf} [14]	2.1	$J \cdot m^{-2}$
Volume diffusion, Q^v [15]	3.2×10^{-19}	J
Surface diffusion, D_0^s [15]	2.92×10^{-19}	$m^2 \cdot s^{-1}$
Surface diffusion coefficient, D_{eff}^s [16]	2×10^{-9}	$m^2 \cdot s^{-1}$
Preheating temperature, T	1100	°C

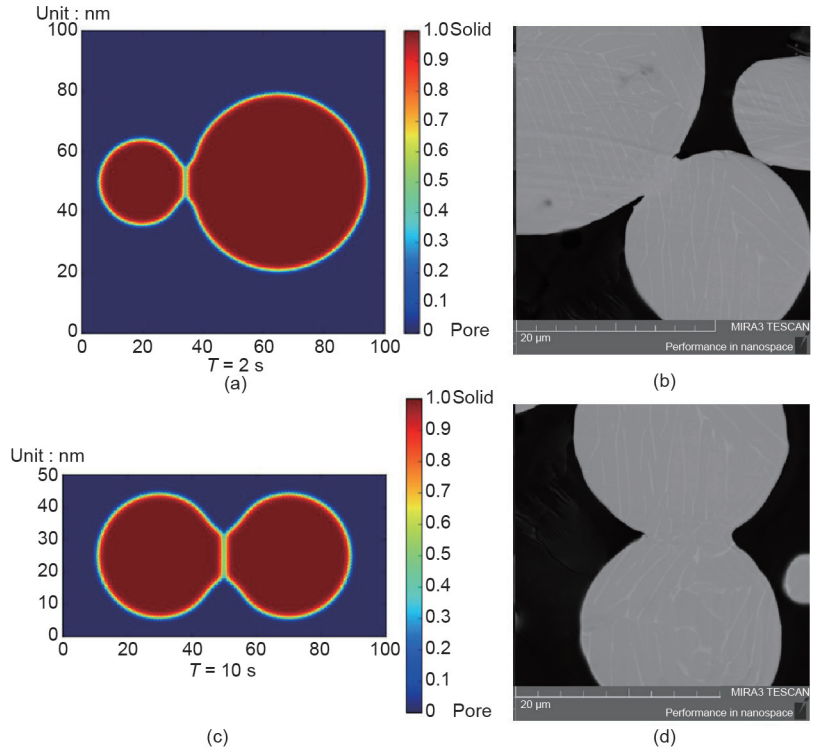

Fig. 6. Experimental and simulation results of powder sintering. (a), (b) two powder particles with different sizes; (c), (d) two powder particles with similar sizes.

4.3. Powder melting

One important feature of our high-fidelity powder-melting model is the accurate implementation of the heat source model by accurately capturing and reconstructing the material surfaces employing an enhanced VOF method [17]. To illustrate this, we simulated the process of an electron beam (in which the energy is evenly distributed within the beam's cross-section) heating a spherical powder particle on a substrate. In Fig. 7, it can be seen that the electron beam can penetrate through the edge of the particle into the substrate below, since the maximum penetration depth of the electron beam is about 16 μm. It is also noted that the subsurface regions (about 5 μm below the surface) have a higher temperature than the surface, thus perfectly incorporating the energy distribution along the penetration depth from the microscale simulation of electron-atom interactions [11,12]. Moreover, in Fig. 7(b), the red region (with a temperature higher than 1928 K) becomes smaller with the increase of distance from the center, because the energy absorptivity is higher near the center and lower near the edge, due to the influence of the incidence angle [12].

The single track acts as one fundamental building unit and largely influences the final product quality, such as the surface roughness and dimensional accuracy. We employed the FVM-based high-fidelity powder-scale model to predict the detailed formation processes of single-track defects, including the balling effect and single-track non-uniformity (Fig. 8). These processes are difficult to observe in experiments; previous studies have proposed different or even conflicting explanations. The model helped clarify the underlying formation mechanisms, reveal the influence of key factors, and guide the improvement of fabrication quality. More detailed discussion and description are in our previous papers [13].

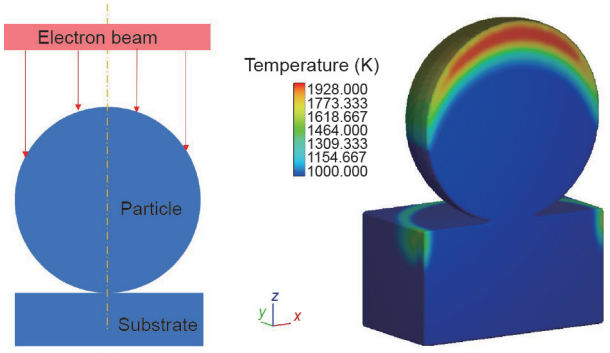

Fig. 7. Simulation result of an electron beam heating a spherical powder particle on a substrate. (a) Schematic; (b) simulated.

The major conclusions are:

- The balling effect is caused by a lack of melting of the substrate under the melted particles. Driven by the surface energy, some of the melted particles merge together into isolated clusters rather than spreading over the unmelted substrate surface.
- The single-track non-uniformity is due to the random attachment of the molten pool to the partially melted particles near the boundaries. In multiple-layer multiple-track manufacturing processes, the previous layers and tracks, as well as the ejected materials, will also influence the non-uniformity of the melt track. The detailed simulation results and discussion are out of the scope of this paper, and can be found in our previous papers [13].

5. Summary

To achieve a comprehensive understanding of the physical mechanisms in the EBSM process, we leverage modeling and experiments. The models consist of ① a powder-spreading model using the DEM, ② a PF model of powder sintering, and ③ a powder-melting model using the FVM. These models fully resemble the actual fabrication procedures. Preliminary simulation results agree qualitatively with experiments, and demonstrate appealing potential to shed light on the underlying mechanisms and to guide the design and optimization of experimental setup and manufacturing processes.

Acknowledgements

The authors at Tsinghua University acknowledge the financial support by the National Key R&D Program of China(2017YFB1103303) and the Suzhou-Tsinghua Innovation Leading Action Specials (2016SZ0216). Yongxing Shen acknowledges the financial support by the Recruitment Program of Global Experts.

Compliance with ethics guidelines

Wentao Yan, Ya Qian, Weixin Ma, Bin Zhou, Yongxing Shen, and Feng Lin declare that they have no conflict of interest or financial conflicts to disclose.

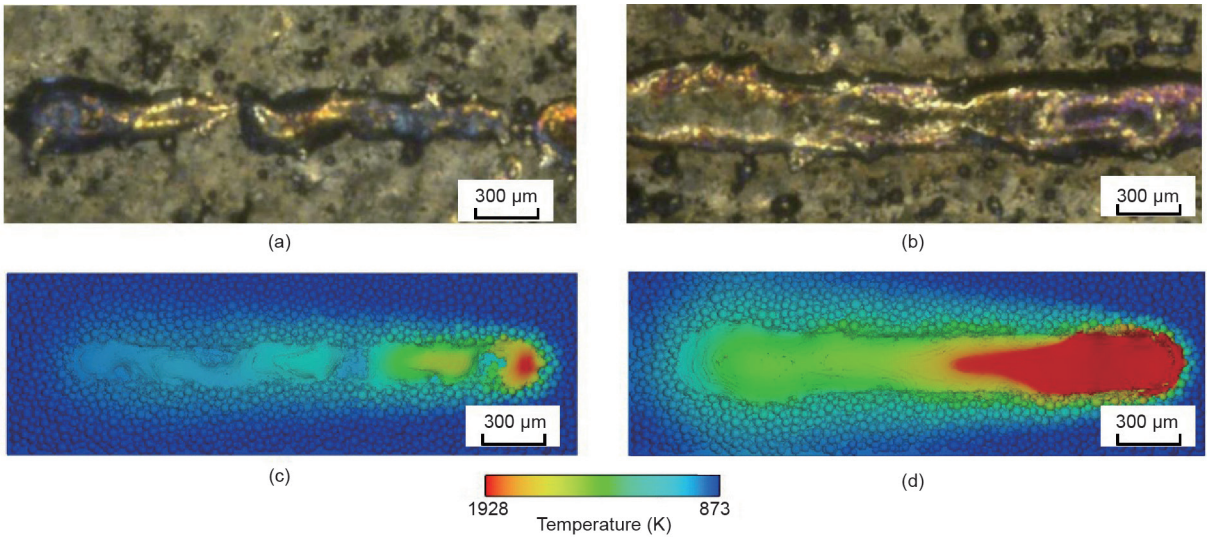

Fig. 8. Experimental and simulation results of (a) and (c) balling effect; and (b) and (d) single-track non-uniformity [13].

References

[1] Yang L, Harrysson O, West H, Cormier D. Compressive properties of Ti–6Al–4V auxetic mesh structures made by electron beam melting. Acta Mater 2012;60(8):3370–9.

[2] Ge W, Lin F, Guo C. Functional gradient material of Ti-6Al-4V and γ-TiAl fabricated by electron beam selective melting. In: Proceedings: 26th Annual International Solid Freeform Fabrication Symposium—An additive manufacturing conference; 2015 Aug 10–12; Austin, Texas; 2015. p. 602–13.

[3] Ge W, Guo C, Lin F. Microstructures of components synthesized via electron beam selective melting using blended pre-alloyed powders of Ti6Al4V and Ti45Al7Nb. Rare Met Mater Eng 2015;44(11):2623–7.

[4] Guo C, Ge W, Lin F. Dual-material electron beam selective melting: Hardware development and validation studies. Engineering 2015;1(1):124–30.

[5] Körner C, Bauereiß A, Attar E. Fundamental consolidation mechanisms during selective beam melting of powders. Model Simul Mater Sci Eng 2013;21(8):085011.

[6] Khairallah SA, Anderson AT, Rubenchik A, King WE. Laser powder-bed fusion additive manufacturing: Physics of complex melt flow and formation mechanisms of pores, spatter, and denudation zones. Acta Mater 2016;108:36–45..

[7] King W, Anderson AT, Ferencz RM, Hodge NE, Kamath C, Khairallah SA. Overview of modelling and simulation of metal powder bed fusion process at Lawrence Livermore National Laboratory. Mater Sci Technol 2015;31(8):957–68.

[8] Qiu C, Panwisawas C, Ward M, Basoalto HC, Brooks JW, Attallah MM. On the role of melt flow into the surface structure and porosity development during selective laser melting. Acta Mater 2015;96:72–9.

[9] Cahn JW, Hilliard JE. Free energy of a nonuniform system. I. Interfacial free energy. J Chem Phys 1958;28(2):258–67.

[10] Alnæs MS, Blechta J, Hake J, Johansson A, Kehlet B, Logg A, et al. The FEniCS Project version 1.5. Arch Numer Softw 2015;3(100):9–23.

[11] Yan W, Smith J, Ge W, Lin F, Liu WK. Multiscale modeling of electron beam and substrate interaction: A new heat source model. Comput Mech 2015;56(2):265–76.

[12] Yan W, Ge W, Smith J, Lin S, Kafka OL, Lin F, et al. Multi-scale modeling of electron beam melting of functionally graded materials. Acta Mater 2016;115:403–12.

[13] Yan W, Ge W, Qian Y, Lin S, Zhou B, Liu WK, et al. Multi-physics modeling of single/multiple-track defect mechanisms in electron beam selective melting. Acta Mater 2017;134:324–33.

[14] Roth TA, Suppayak P. The surface and grain boundary free energies of pure titanium and the titanium alloy Ti–6Al–4V. Mater Sci Eng 1978;35(2):187–96.

[15] Nemat-Nasser S, Guo WG, Cheng JY. Mechanical properties and deformation mechanisms of a commercially pure titanium. Acta Mater 1999;47(13):3705–20.

[16] Sushko GB, Verkhovtsev AV, Yakubovich AV, Schramm S, Solov'yov AV. Molecular dynamics simulation of self-diffusion processes in titanium in bulk material, on grain junctions and on surface. J Phys Chem A 2014;118(33):6685–91.

[17] Barkhudarov MR. Lagrangian VOF advection method for FLOW-3D®. Leland: Flow Science, Inc.; 2004 Jun. Report No.: FSI-03-TN63-R.